Angewandte Chemie

Angewandte Chemie GDCh German Chemical Society

Zitierweise: *Angew. Chem. Int. Ed.* **2026**, 65, e6295065
doi.org/10.1002/anie.6295065

FORSCHUNGSARTIKEL

Grain-Oriented Dissolution Enabled by Hydrogel for Highly Reversible Zn Anodes

Zixing Dong[1] | Shige Wang[2,3] | Jiashu Chen[4] | Qianwei Huang[1] | Haoqing Ji[5] | Jun Peng[6] | Huakun Liu[1] | Jingyu Sun[5] | Shixue Dou[1] | Lizhi Xu[2] | Zaiping Guo[7] | Chao Wu[1] | Xianzhong Yang[1]

[1]Institute of Energy Materials Science (IEMS), University of Shanghai for Science and Technology, Shanghai, P. R. China | [2]Department of Mechanical Engineering, The University of Hong Kong, Hong Kong SAR, P. R. China | [3]School of Materials and Chemistry, University of Shanghai for Science and Technology, Shanghai, P. R. China | [4]Department of Mechanical Engineering, The Hong Kong Polytechnic University, Hong Kong SAR, P. R. China | [5]College of Energy, Soochow Institute for Energy and Materials Innovations, Soochow University, Suzhou, P. R. China | [6]Center For Hybrid Nanostructures, University of Hamburg, Hamburg, Germany | [7]Department of Materials Science and Engineering, City University of Hong Kong, Hong Kong, P. R. China

Correspondence: Lizhi Xu (xulizhi@hku.hk) | Zaiping Guo (zaiping.guo@adelaide.edu.au) | Chao Wu (chaowu@usst.edu.cn) | Xianzhong Yang (xzhyang@usst.edu.cn)

Received: 6 February 2026 | **Revised:** 15 April 2026 | **Accepted:** 21 April 2026

Keywords: grain-oriented stripping | hydrogel electrolyte | uniform deposition | Zn anodes | Zn-ion batteries

ABSTRACT

The reversibility of Zn anodes is severely compromised by dendritic growth and parasitic hydrogen evolution reactions. Directing Zn to undergo grain-oriented stripping offers an effective approach to mitigating these issues. However, this strategy has rarely been explored, and the underlying mechanism remains unclear. Herein, we design a multifunctional hydrogel composed of aramid nanofiber-polyvinyl alcohol (ANF-PVA) and calcium lignosulfonate (LS) to dynamically regulate the anode interface. The ANF-PVA hydrogel framework possesses excellent mechanical stability and a uniform porous structure that promotes a homogeneous electric field distribution. Concurrently, the incorporated LS preferentially adsorbs onto specific Zn crystal planes, which equilibrates the stripping energy barrier. Through the synergistic regulation between ANF-PVA and LS, grain-oriented dissolution is achieved. The in situ formed solid electrolyte interphase (SEI) can further guide uniform Zn deposition and effectively suppress side reactions. Consequently, Zn||Zn symmetric cells exhibit exceptional cycling stability under both ambient (5000 h at 2 mA cm^{-2}/1 mAh cm^{-2}) and low-temperature conditions (10 900 h at −40 °C). The Zn||I$_2$ full cell achieves 78.2% capacity retention after 20 000 cycles at 5 A g^{-1}. Remarkably, pouch-type cells also sustain 700 cycles. This work opens a new avenue for achieving highly reversible Zn anodes through grain-oriented dissolution.

1 | Introduction

With the global shift towards renewable energy, the demand for safe, cost-effective, and efficient energy storage systems has become increasingly pressing [1–3]. Although lithium-ion batteries dominate portable electronics and electric vehicles, their high cost and safety concerns restrict their suitability for large-scale grid storage [4–7]. In contrast, aqueous Zn-ion batteries (AZIBs) present notable advantages including high safety, low cost, environmental benignity, and a high theoretical capacity, positioning them as a promising next-generation energy storage technology [8–11]. However, the practical deployment of AZIBs is still impeded by dendrite growth and parasitic reactions of Zn anodes [12–14]. These issues stem mainly from uneven Zn

---

Zixing Dong, Shige Wang and Jiashu Chen contributed equally to this work.

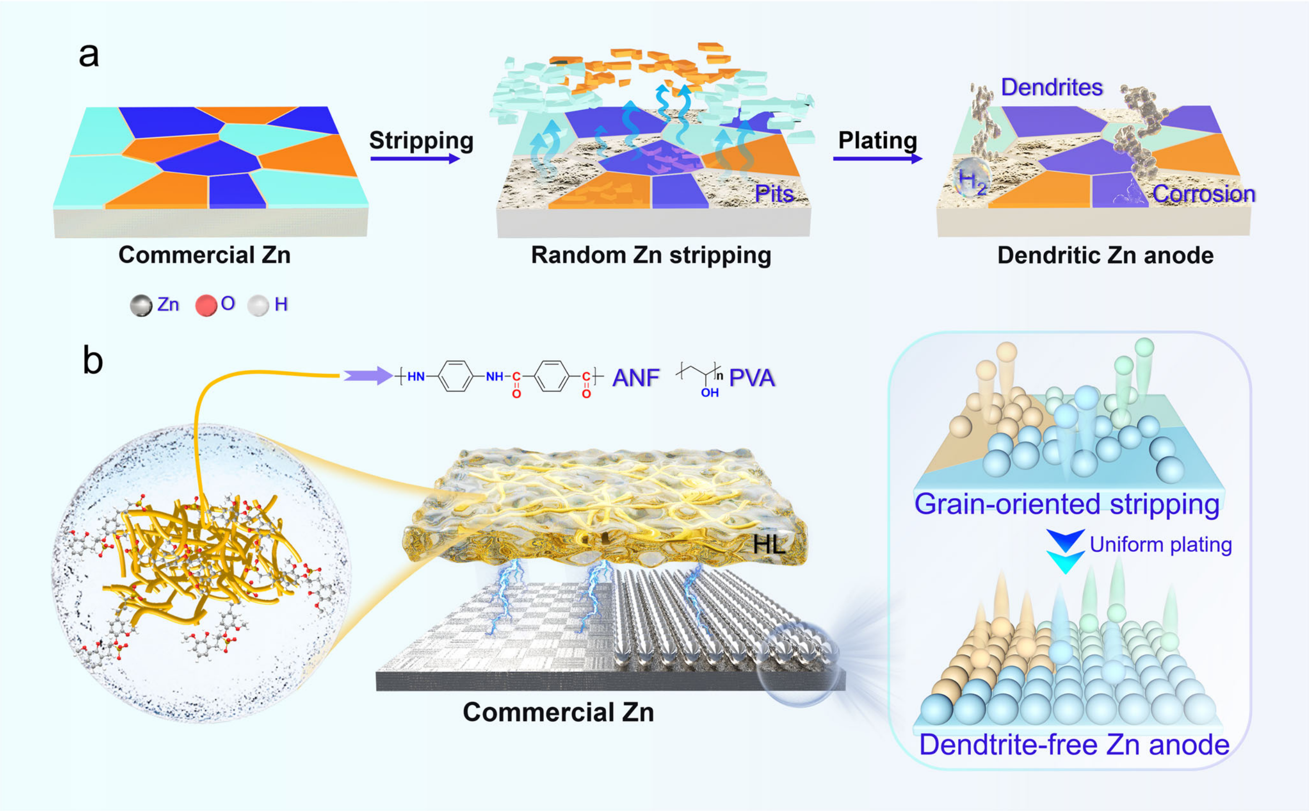

FIGURE 1 | Schematic of (a) issues induced by stripping and (b) the stripping/plating process in HL electrolyte.

deposition and stripping during cycling, which cause morphological degradation and poor reversibility. Achieving controllable interfacial reactions and uniform morphological evolution at the Zn anode is thus a key challenge toward the commercialization of AZIBs.

Crystallographic manipulation along specific crystal planes facilitates the formation of compact Zn layers while simultaneously suppressing adverse side reactions [15, 16]. To date, a variety of strategies have been devised to regulate the crystal orientation during Zn deposition, including homoepitaxial deposition [3, 17, 18], heteroepitaxial deposition [19–21], crystal facet anchoring [22], and current density modulation [23]. By contrast, the stripping process has received far less attention. Indeed, the homogeneity of Zn stripping critically determines the morphology of subsequent deposition [24–26]. Non-uniform Zn dissolution results in the accumulation of “dead Zn”, which reduces Coulombic efficiency (CE) and causes capacity decay. Meanwhile, the resulting rough surface morphology further aggravates dendrite growth and parasitic side reactions. The inhomogeneity of deposition and stripping mutually reinforce each other, creating a self-amplifying degradation cycle (Figure 1a). In response, recent studies have proposed “stripping-guided” strategies to address these challenges. For instance, Guo et al. demonstrated that a Cu@Zn alloy interlayer can modulate Zn stripping behavior [27]. Similarly, Zhang et al. developed an electrolyte additive strategy to dynamically regulate the stripping and deposition processes [28]. Although some progress has been made in current research on Zn stripping, crystallographic regulation of the stripping process remains elusive. Commercial Zn foil is a polycrystalline structure assembled from grains with different sizes and orientations. Layer-by-layer Zn stripping along specific grain orientations, a process termed as grain-oriented stripping, can ensure perfectly flat dissolution, thereby ensuring subsequent uniform deposition. Therefore, achieving grain-oriented stripping is highly desirable for practical Zn anodes, yet it is still rarely reported.

Herein, we report a calcium lignosulfonate (LS) modified aramid nanofiber-polyvinyl alcohol (ANF-PVA) hydrogel electrolyte (HL) to dynamically regulate the stripping behavior. The nanoporous ANF-PVA network provides efficient Zn^{2+} transport pathways and promotes a uniform electric field distribution, which equalizes the overpotential for Zn dissolution from a kinetic perspective. The sulfonate-rich LS preferentially adsorbs onto the electrode surface, thermodynamically leveling the dissolution energy. This synergistic regulation between ANF-PVA and LS enables the grain-oriented stripping. Additionally, the decomposition of LS forms an in situ SEI enriched with organic phase, which further induces uniform plating and maintains the grain-oriented stripping process (Figure 1b). Leveraging the dynamic interfacial regulation of HL, Zn||Zn symmetric cells achieve outstanding cycling stability across a wide range of conditions: over 5000 h at 2 mA cm^{-2}/1 mAh cm^{-2}, over 1200 h at 5 mA cm^{-2}/5 mAh cm^{-2}, and exceeding 10 900 h even at −40 °C with a current density of 0.5 mA cm^{-2}. The Zn||I_2 full cell also delivers superior rate capability and durability, retaining 78.2% of its capacity after 20 000 cycles at 5 A g^{-1}. This work provides a new paradigm for designing functional hydrogel electrolytes for reversible Zn anodes.

2 | Results and Discussion

2.1 | Electrolyte Design and Basic Properties

The ANF-PVA hydrogel was prepared according to a reported procedure with slight modifications [29]. Briefly, pre-synthesized ANF and PVA were separately dissolved in DMSO at mass fractions of 2 and 15 wt%, respectively [30]. The two solutions were mixed in a 1:1 weight ratio, cast into molds, and then immersed in deionized water for solvent exchange to form the final hydrogel (Figure S1). This procedure yields a 3D nanoporous network that serves as the mechanical framework of the composite electrolyte. Scanning electron microscopy (SEM) images reveal that the hydrogel consists of highly interconnected nanofibers with uniform porosity (Figure 2a), which facilitates homogeneous Zn^{2+} transport. The obtained ANF-PVA hydrogel was immersed in a $Zn(ClO_4)_2$ solution containing LS for 4 h to yield the target hydrogel electrolyte, denoted as HL (Figure S2), while the hydrogel electrolyte without additive was labeled as HE. Quantitative data indicate that the HL electrolyte reached swelling equilibrium within 15 h of immersion (Figure S3), exhibiting a weight increase of 900% and a thickness variation of 550%. This low swelling ratio endows HL with exceptional structural stability, which is highly beneficial for stable battery cycling. Furthermore, the introduction of LS markedly enhances the electrolyte's affinity for the Zn anode (Figure S4), primarily due to the strong adsorption of LS onto the Zn surface [31]. The ANF-PVA hydrogel demonstrates excellent flexibility and stretchability, as evidenced in Figures S5,S6. Furthermore, stress–strain results indicate that HL shows much higher tensile strength than the pristine ANF-PVA hydrogel or LE (Figure 2b), which may be attributed to the strong interaction between the LS and the ANF-PVA matrix. Here, the stress–strain curve for LE corresponds to glass fiber soaked with $Zn(ClO_4)_2$ solution. Fourier transform infrared spectroscopy was used to further investigate the structural features of HL and HE (Figure 2c). A distinct spectral contrast is observed in the ClO_4^- region (1071–1154 cm^{-1}), where HE shows a broad envelop while HL exhibits resolved peaks, corresponding to the symmetric and asymmetric stretching vibrations of the $-SO_3^-$ groups. Notably, the introduction of ANF-PVA and LS markedly intensifies the absorption of strong hydrogen bonds at 3225 cm^{-1}, increasing its proportion from 13.2% to 23.9% compared to that in LE (Figures 2d,S7). This alteration disrupts the native hydrogen-bonding network of water, thereby reducing the activity of free water and preventing ice crystal formation, which collectively enhance the anti-freezing performance of the solution [32]. Differential scanning calorimetry further substantiates this improvement, revealing that the HL electrolyte exhibits a significantly depressed freezing point (−72.3° C) relative to the pristine $Zn(ClO_4)_2$ liquid electrolyte (LE, Figures 2e,S8). The conventional $ZnSO_4$ solution, by comparison, freezes at only −34 °C, making it highly susceptible to low temperatures. This vulnerability directly motivated our selection of $Zn(ClO_4)_2$ as the primary salt in the electrolyte. These results underscore the considerable potential of the HL electrolyte for low-temperature operation. Nuclear magnetic resonance spectra show a gradual downfield shift of the H peak with increasing LS content, indicating enhanced proton deshielding. This is attributed to the stronger local electric field or hydrogen-bond network established upon LS coordination, which imposes greater deshielding on water protons and thereby lowers water activity (Figure 2f).

Molecular dynamics (MD) simulations offer further mechanistic validation. As shown in the snapshots (Figures 2g,S9), Zn^{2+} ions in the LE system are surrounded by approximately six H_2O molecules, forming a typical first solvation shell, as evidenced by a pronounced radial distribution function (RDF) peak at 2.14 Å for $Zn-O$ (H_2O). In contrast, in the HL system, partial water molecules are replaced by $-SO_3^-$ groups, giving rise to $Zn^{2+}-O(SO_3^-)$ interactions with a characteristic RDF peak at ~2.08 Å. Consequently, the coordination number of $Zn-O(H_2O)$ decreases from 6.05 to 5.10 (Figure 2h), resulting in a new solvation structure of $Zn^{2+}[H_2O]_5[LS]_1$. The reduction in coordinated water molecules helps suppress the hydrogen evolution reaction (HER). To investigate the influence of hydrogel thickness on electrochemical performance, HL membranes with different thicknesses were assembled into Zn||Zn symmetric cells for galvanostatic cycling (Figures S10,S11). Based on the results, an optimized thickness of 53 µm was selected for subsequent studies unless otherwise specified. Owing to its uniform porous structure, HL shows a higher ionic conductivity (24.3 mS cm^{-1}) than LE (14.0 mS cm^{-1}, Figure S12), which is beneficial for the reaction kinetics. Electrostatic potential mapping (Figures 2i,S13) shows that the polar sulfonate groups in HL possess a high electronegativity, which facilitates the attraction of Zn^{2+} and the establishment of continuous Zn^{2+} transport channels, thereby enhancing ion transport kinetics [33]. Binding energy calculations provide further insight into the interactions among the components in the HL system. As shown in Figure S14, compared with ANF-PVA, LS, and ClO_4^-, Zn^{2+} exhibits the lowest binding energy with H_2O. This indicates that the LS and the hydrogel framework can readily reconstruct the solvation structure of Zn^{2+} through strong competitive coordination, thereby regulating the deposition and stripping behavior. The value of −0.460 kJ mol^{-1} between H_2O and LS reflects LS's strong H_2O affinity (Figure 2j), enabling it to immobilize free water via hydrogen bonding and electrostatic interactions. The LS–ANF-PVA pair exhibits the strongest binding (−1.316 kJ mol^{-1}), far surpassing other pairs, which confirms their tight coupling. Additionally, the interactions of ClO_4^- with LS and ANF-PVA contribute to anion fixation and facilitate cation migration. As a result, the Zn^{2+} transference number of HL (0.869) is significantly higher than that of LE (0.186, Figure S15), a property that is advantageous for mitigating anion-driven side reactions. These results collectively demonstrate that, the ANF-PVA scaffold offers a uniform porous architecture for efficient ion transport. Moreover, the robust interactions of both ANF-PVA and LS with water and Zn^{2+} reduce the freezing point of the electrolyte and facilitate cation migration, thereby improving the overall electrochemical performance.

2.2 | Bidirectional Zn Plating/Stripping Regulation

To elucidate the influence of HL on the morphological evolution of Zn anodes during cycling and to decouple the respective contributions of ANF-PVA and LS, a series of microscopic characterizations were conducted. First, a Zn||Zn symmetric cell was subjected to one single charge-discharge at 10 mA cm^{-2}/1 mAh cm^{-2} to capture the resulting surface morphologies. In comparison to glass fiber (GF, Figures 3a,S16) separator, the ANF-PVA hydrogel exhibited a relatively smooth surface (Figure 3b), although some small pits were still visible. This

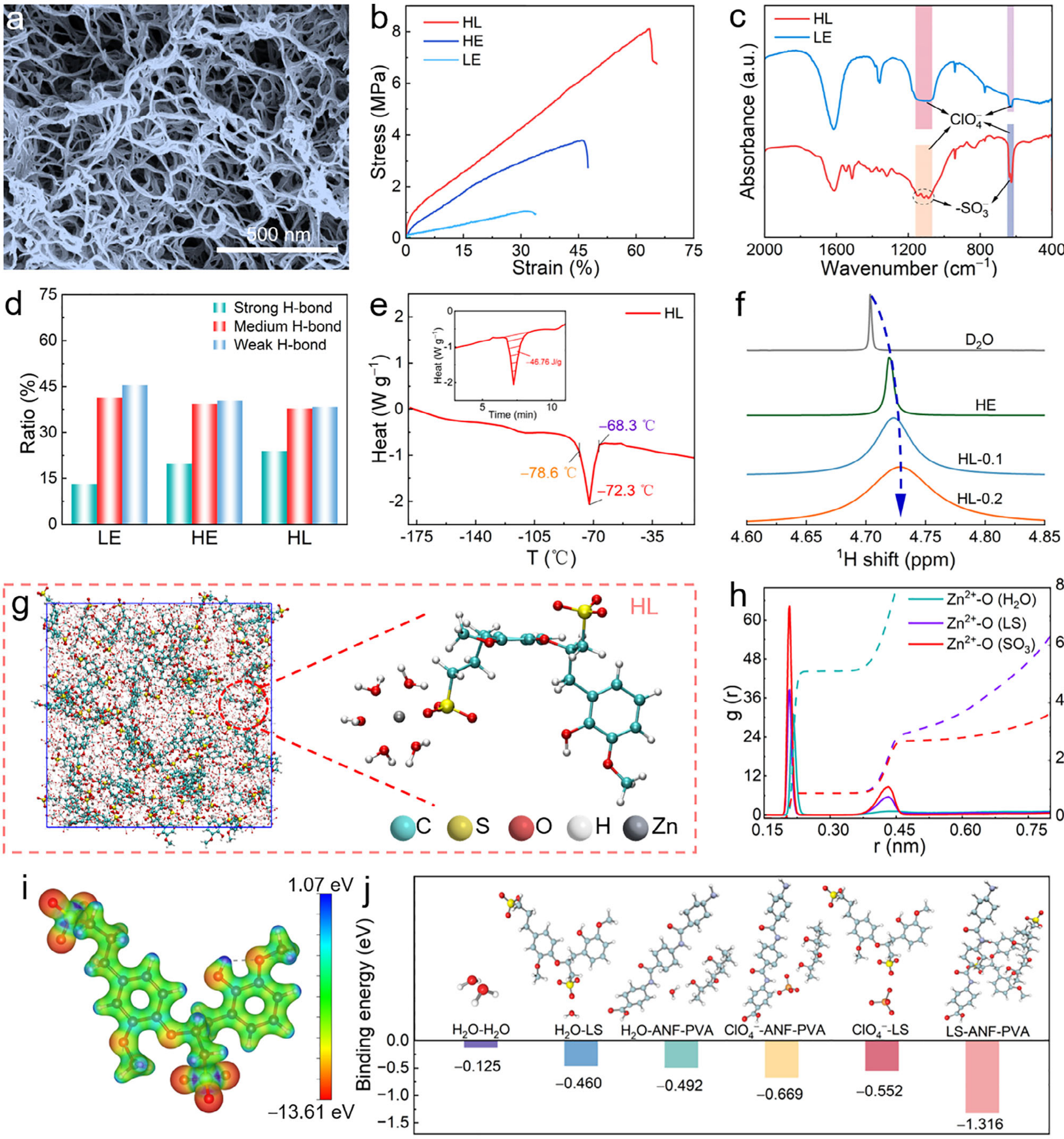

FIGURE 2 | Characterization of HL electrolyte. (a) SEM image of the ANF-PVA hydrogel prepared with supercritical CO_2 drying. (b) Stress–strain curves of ANF-PVA hydrogel. (c) Comparison of Fourier transform infrared spectroscopy spectra. (d) Ratios of strong H-bond, medium H-bond, and weak H-bond. (e) Differential scanning calorimetry curve for HL electrolyte. (f) Nuclear magnetic resonance of different solutions with deuterated water as solvent. (g) The MD snapshots of HL electrolyte. (h) The RDF and coordination number of HL. (i) Electrostatic potential maps of the LS molecule. (j) Calculated binding energies for different molecules.

indicates that a single hydrogel scaffold alone is insufficient to completely prevent excessive local dissolution. Encouragingly, the introduction of LS can significantly improve the exfoliation morphology. When GF was matched with LS, partial stripping along the grain direction could be observed (Figure 3c). However, due to the absence of ANF-PVA to continuously maintain a stable interface environment, this local regulation becomes unstable and gradually deteriorates over long-term cycling. Impressively, grain-oriented peeling along the grain direction was achieved when LS and ANF-PVA was used together (Figures 3d, e, and S17), confirming the synergistic effect of LS and ANF-PVA in promoting uniform Zn stripping. Moreover, the deposited Zn layer also displayed a highly flat morphology (Figure S18). Even after 75 cycles (Figures 3f,S19) and up to 600 cycles at 10 mA cm^{-2} (Figure S20), the electrode in HL retained grain-defined stripping features and preserved dense deposition layers. The same phenomenon

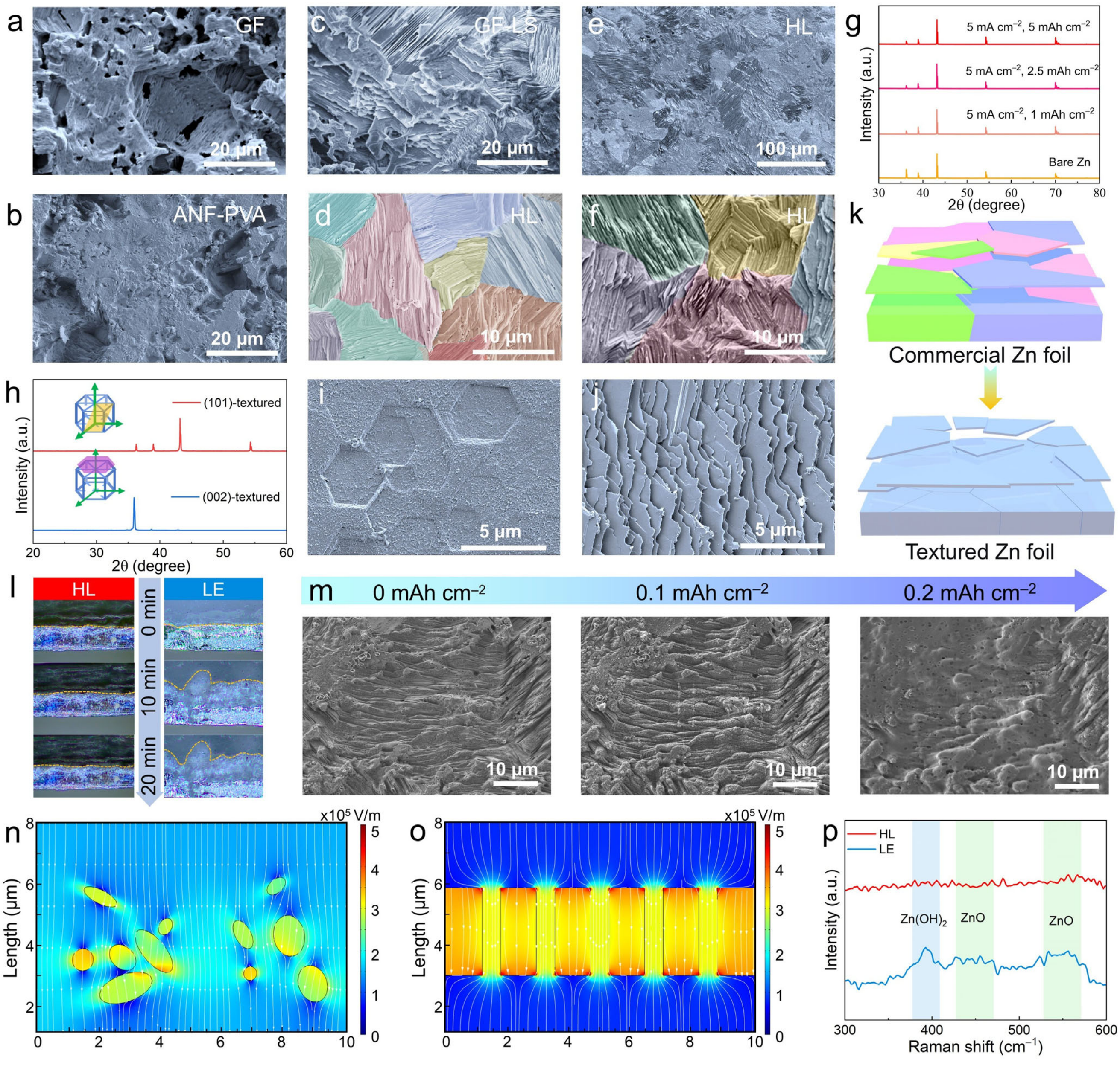

FIGURE 3 | Characterization of Zn stripping/plating patterns. SEM images of Zn electrode after stripping at 10 mA cm^{-2}/1 mAh cm^{-2} within (a) GF, (b) ANF-PVA, (c) GF-LS, and (d, e) HL. (f) SEM image of the stripped Zn electrode after 75 cycles in HL electrolyte. (g) XRD patterns of the Zn electrode recorded after stripping at different capacities in the HL electrolyte. (h) XRD patterns of the textured Zn foil. SEM images of the (i) (002)- and (j) (101)-textured Zn electrodes after stripping for 1 mAh cm^{-2}. (k) Schematic diagram showing the stripping behavior of commercial and textured Zn electrodes. (l) In situ optical microscopy observation of Zn plating within HL and LE. (m) SEM images of stripped Zn before and after further plating. Simulated electric field distribution of the Zn electrodes in (n) LE and (o) HL. (p) Raman spectra of Zn electrodes after the first stripping within different electrolytes.

was also observed under high depth of discharge conditions (5–10 mAh cm^{-2}, Figure S21). Conversely, the electrode in LE consistently developed irregular pits and protrusions (Figure S22). The x-ray diffraction (XRD) patterns collected at different stripping capacities showed that the intensity ratios of the characteristic peaks remained relatively constant, suggesting a grain-oriented stripping mechanism (Figure 3g). In order to better verify the oriented peeling phenomenon of Zn along different crystal planes, we employed heat treatment technology to texture commercial Zn foil [11], enabling the study of stripping behavior on a single crystal plane, specifically Zn(002) and Zn(101) (Figure 3h). On the Zn(002)-textured foil, stripping results in the formation of highly regular hexagonal pits (Figures 3i,S23a), which perfectly align with the inherent sixfold symmetry of Zn's hexagonal close-packed lattice along the c-axis. Similarly, on the Zn(101)-textured foil (Figures 3j,S23b), the stripping morphology exhibits highly directional stripe-like arrays, consistent with the characteristic atomic step arrangement of the (101) plane. Obviously, the dissolution morphology of textured Zn is strictly governed by its intrinsic crystallographic orientation within HL system. In contrast, after cycling the textured Zn electrode in the LE system, the original textured structure was completely destroyed (Figure S24). Therefore, the HL electrolyte enables layer-by-layer stripping along the crystallographic orientation of the original grains, effectively eliminating the severe anisotropic dissolution observed in LE. As a result, it achieves grain-oriented stripping in both commercial polycrystalline Zn and textured Zn foil (Figure 3k). For a stable Zn anode, both the stripping and deposition behaviors of Zn are crucial. In situ optical microscopy was used to further visualize the dynamic evolution of Zn deposition. It revealed that the Zn deposition interface in the HL system maintained a smooth and uniform morphology under galvanostatic discharge conditions (Figure 3l). In sharp contrast, the LE system exhibited pronounced dendritic protrusions with increasing deposition capacity, highlighting the beneficial role of HL in regulating Zn deposition behavior. Interestingly, the HL membrane maintained tight adhesion to the Zn substrate after electrodeposition (Figure S25). This intimate interfacial contact is essential for guiding reversible stripping/plating. To evaluate the effect of grain-oriented stripping on subsequent plating, gradient deposition (0–0.5 mAh cm^{-2}) was performed on Zn samples after stripping 1 mAh cm^{-2}. Unlike the rough and corroded surface in the LE system, the electrode surface in the HL progressively developed a uniform compact layer, culminating in a fully dense morphology at about 0.5 mAh cm^{-2} (Figures 3m,S26). This dense stripping/plating helps to inhibit the formation of by-products. Chronoamperometry (Figure S27) provided additional insights for uniform Zn deposition: Zn in HL rapidly transitioned from two-dimensional (2D) to three-dimensional (3D) diffusion process, whereas Zn in LE remained confined to 2D diffusion.

To gain further insight into the kinetic mechanism of grain-oriented stripping, we employed COMSOL simulations to compare the electric field distributions in the LE and HL systems. In the LE system (Figure 3n), the randomly intertwined GF creates pore structures of varying sizes, which leads to an uneven interfacial electric field. Regions of high electric field intensity exhibit increased overpotential and faster charge transfer, where Zn atoms preferentially lose electrons and dissolve into the electrolyte. This localized preferential dissolution rapidly leads to pit formation. These pits subsequently serve as primary precursors for dendritic growth during plating. Benefiting from its porous structure and excellent interfacial wettability, the HL electrolyte ensures a highly uniform electric field at the Zn/HL interface (Figure 3o). This equalizes the overpotential across the electrode surface, placing all exposed Zn atoms under the same oxidation driving force. The absence of preferential dissolution “hot spots” leads to synchronous Zn dissolution, thereby creating favorable conditions for subsequent homogeneous redeposition (Figure S28). Apart from the electric field regulation, the chemical stability of the interface after stripping was examined by Raman spectroscopy (Figure 3p). Strong ZnO and $Zn(OH)_2$ peaks were identified on the Zn electrode in LE, whereas no detectable by-product signals were found in HL. This absence of parasitic by-products directly corroborates the by-product inhibition mentioned earlier and underscores the effectiveness of HL in mitigating corrosion.

2.3 | Composition and Structure of the SEI

Aiming at probing the evolution of chemical components on the electrode surface during Zn deposition, detailed transmission electron microscopy (TEM) characterizations were conducted. As clearly illustrated in Figure 4a, the sample prepared within the HL electrolyte exhibits a well-defined SEI layer approximately 50 nm thick on its outer surface, whereas the LE based counterpart presents an uneven edge devoid of discernible SEI characteristics (Figure 4b). Notably, high-resolution TEM clearly resolves lattice fringes within the interfacial layer (Figure 4c), with measured interplanar spacings of 0.260, 0.292, 0.275, and 0.280 nm across four selected regions. Combined with electrolyte composition and energy-dispersive x-ray spectroscopy (EDS, Figure S29), these spacings are preliminarily assigned to ZnO (002) [34], ZnS (101) [35], $ZnCO_3$ (104) [36], and ZnO (100) [21], respectively. In contrast, the LE-based sample yields lattice spacings of 0.249, and 0.252 nm (Figure S30), predominantly corresponding to Zn (002) and ZnO (002). Subsequently, the spatial distribution of SEI components was scrutinized by in situ depth profiling using Ar^+ sputtering coupled with x-ray photoelectron spectroscopy (XPS) analysis (Figure 4d). Prior to etching, the S 2p spectrum can be deconvoluted into two peaks: A dominant peak at 168 eV ascribed to SO_3^- species and a minor contribution at 161.7 eV attributed to ZnS. Concurrently, the C 1s spectrum reveals pronounced —O/—H signatures, indicative of residual organic fragments originating from incomplete decomposition of LS. As sputtering proceeds, sulfonate signals attenuate while ZnS intensifies, confirming the abundant presence of ZnS within the SEI interior. The C 1s spectrum further reveals a $ZnCO_3$ characteristic peak at 289 eV, with its intensity slightly diminishing upon etching. Concurrently, the fitted peaks at 285.4 eV (—O/—N) and 284.7 eV (—C/—H) show a gradual decrease in intensity during etching, indicating an organic-enriched surface SEI layer. These synchronous variations corroborate that the LS decomposes to form a stable SEI, which is further supported by the O 1s spectrum (Figure S31). The —O component at 531.9 eV primarily arises from $ZnCO_3$, while after 50 s of etching, a ZnO peak emerges at 530 eV. Meanwhile, the Zn 2p spectrum shows a progressive shift of Zn^{2+} peaks (from ZnS, $ZnCO_3$, and ZnO) toward metallic Zn, confirming the formation of a hybrid SEI layer. Analysis of the XPS spectra reveals that the organic phase permeates the entire SEI structure, which is crucial for regulating Zn stripping/plating behavior. As a control, the electrode prepared in LE (Figure S32) exhibits solely ZnO signals, attributable to the inherent strong oxidizability of perchlorate.

To substantiate these findings, time-of-flight secondary ion mass spectrometry (ToF-SIMS) depth profiling was conducted to elucidate the 3D spatial distribution of SEI constituents. As illustrated in Figures 4e and S33, the intensities of organic fragments (CN^-, CH^-, CO_3^-) progressively decline with sputtering depth, in excellent alignment with C 1s results. Similarly, SO^- and ZnS^- signals diminish with depth, whereas ZnO^- exhibits a slower decay, consistent with O 1s spectra. These results demonstrate that, the synergistic oxidative effects of perchlorate and abundant hydroxyl groups in HL promote continuous formation of a ZnO-rich interface layer during the initial electrodeposition stage.

2.4 | Mechanism of Grain-Oriented Stripping and SEI Formation

Density functional theory (DFT) calculations were performed to elucidate the fundamental mechanism of Zn stripping behavior

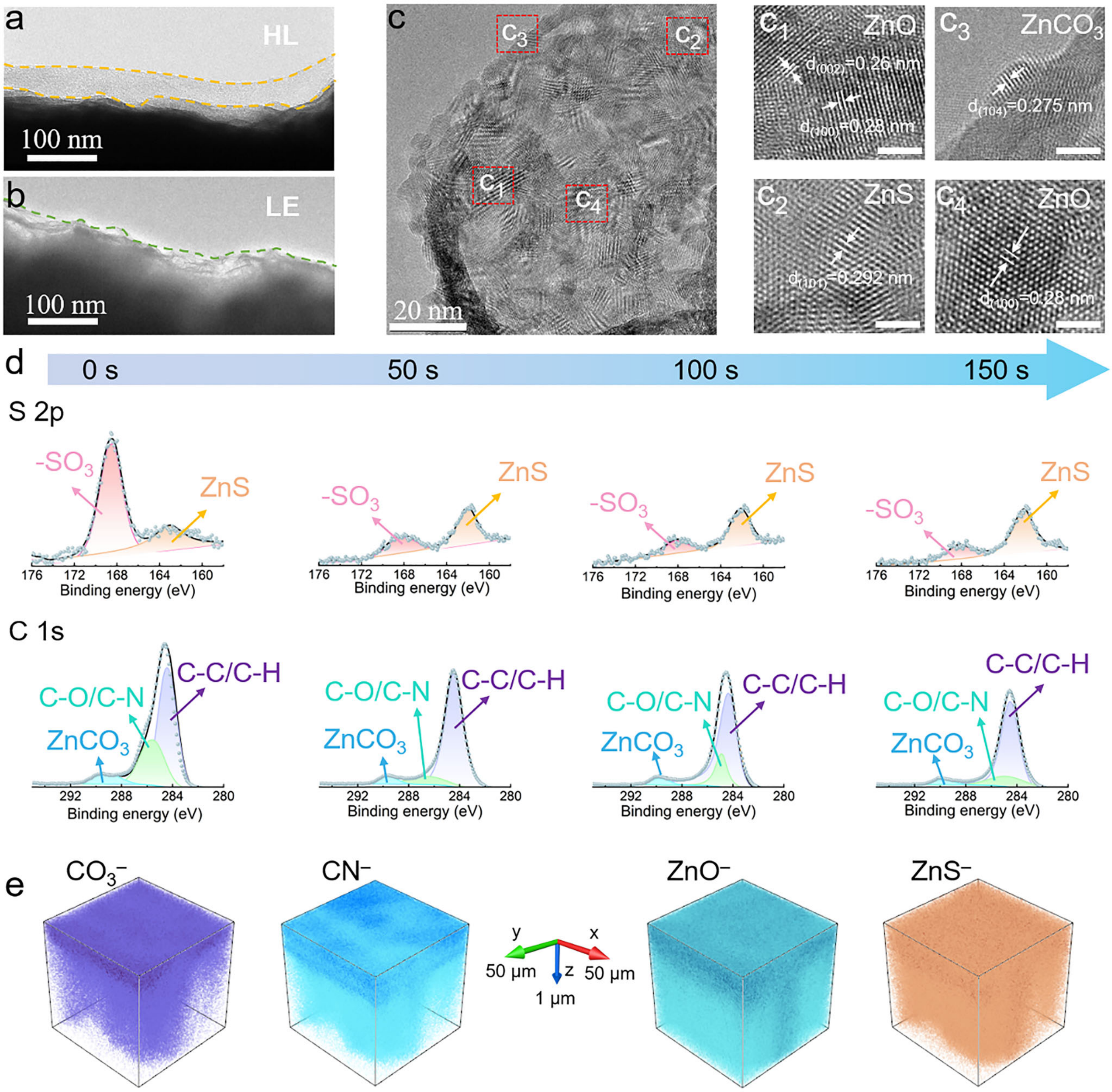

FIGURE 4 | The composition characterization and formation mechanism of SEI. Low-magnification TEM for electrodeposited Zn within (a) HL and (b) LE. (c) High-resolution TEM image of the SEI layer formed in the HL system. Scale bars: 5 nm. (d) S 2p and C 1s XPS spectra with different etching time. (e) Spatial distribution of CO_3^-, CN^-, ZnO^-, and ZnS^- on the Zn anode detected by ToF-SIMS.

regulated by the HL electrolyte. The results demonstrate that the $-SO_3^-$ group exhibits a markedly stronger adsorption affinity for Zn surface compared to water molecules (Figure 5a). The substantial reduction in electric double-layer capacitance observed in the symmetric cells also verifies the favorable adsorption of LS molecules (Figure S34). This interaction is further corroborated by charge-density difference analysis (Figures 5b,S35), which reveals pronounced electron redistribution at the interface following LS adsorption on the Zn(002) surface. Such redistribution indicates strong chemical coupling and electronic hybridization between LS and Zn, thereby enhancing interfacial charge-transfer kinetics. Furthermore, the energy for Zn dissolution was examined across different crystallographic planes. In LE, the process is highly anisotropic, with the (002) facet exhibiting the highest dissolution energy (2.22 eV) and the (101) facet the lowest (1.11 eV). This vast disparity leads to non-uniform stripping. Encouragingly, in the HL electrolyte, the dissolution energies for all facets are substantially reduced and converge to similar values (Figure 5c). The introduction of LS mitigates the crystallographic dependence of Zn dissolution. This thermodynamically promotes uniform stripping and effectively suppresses the formation of pits and "dead-Zn" caused by localized excessive dissolution. Apart from thermodynamic improvement, the HL electrolyte also enhances the interfacial reaction kinetics. As evidenced by Tafel plots (Figure S36), the exchange current density (j_0 = 0.48 mA cm^{-2}) of the HL system exceeds that of the LE (j_0 = 0.38 mA

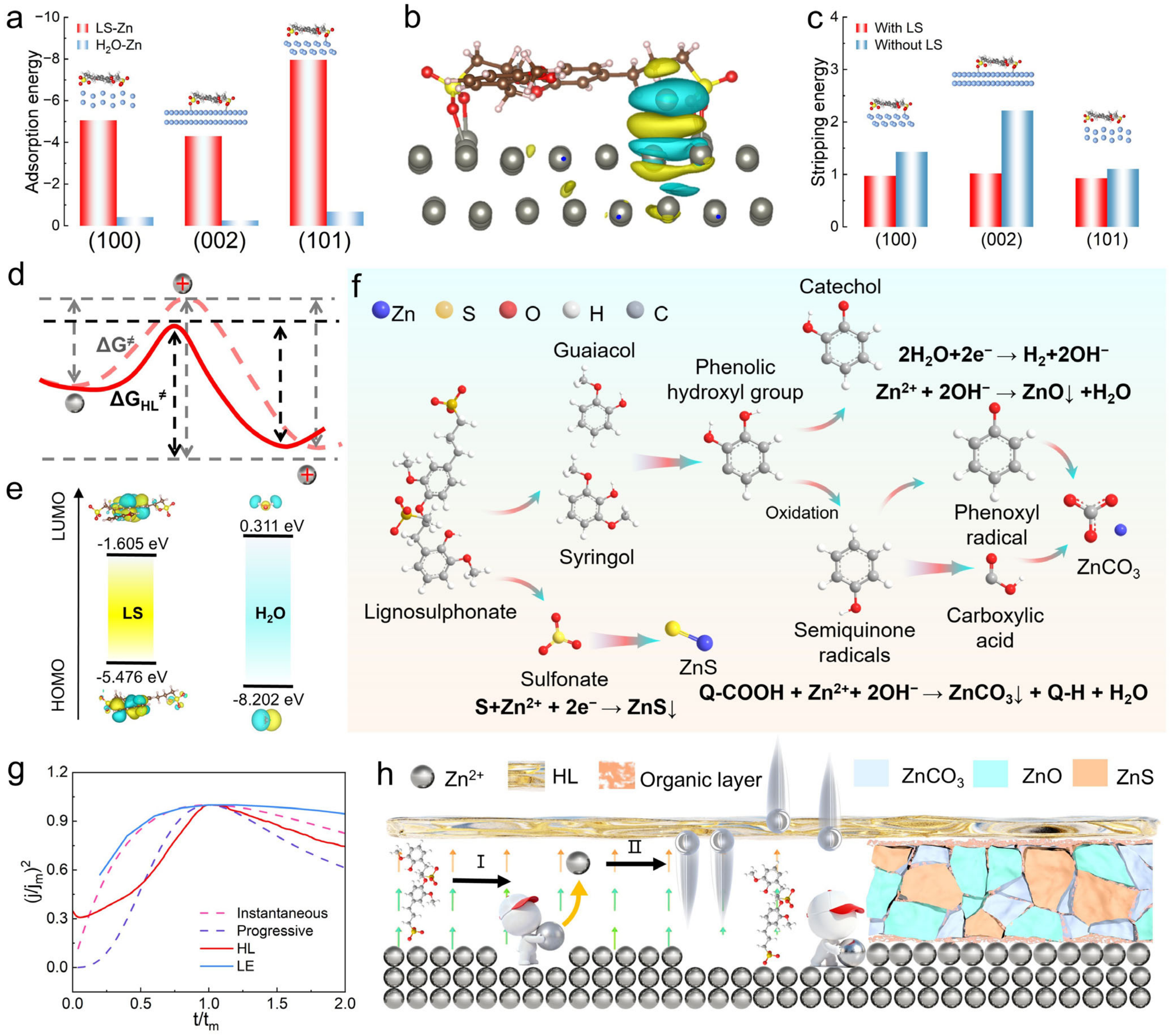

FIGURE 5 | Mechanism of SEI formation and uniform Zn stripping. (a) Adsorption energies of LS and H_2O molecules on Zn(002), (100), and (101) planes. (b) Charge density difference of the adsorbed LS on the Zn(002) surface. (c) Dissolution energy for removing one Zn atom from different surfaces after LS adsorption. (d) Activation Gibbs free energy of the stripping step. (e) LUMO and HOMO isosurfaces of LS and H_2O. (f) Deduced SEI formation pathways. (g) Dimensionless curves for instantaneous and progressive nucleation. (h) Schematic illustration of the SEI formation and uniform stripping/plating process.

cm^{-2}), implying an accelerated electrode reaction rate. According to transition state theory, the exchange current density can be expressed as:

$$j_0 = F\left(\frac{k_B T}{h}\right) C \exp\left(-\frac{\Delta G^{\neq}}{RT}\right)$$

where, j_0 is the exchange current density, F is the Faraday constant, k_B is the Boltzmann constant, T is the absolute temperature, h is the Planck constant, C is the bulk electrolyte concentration, R is the universal gas constant, and $\Delta G^{\neq}$ is the activation energy barrier. From this relationship, it can be derived that an increase in the exchange current density corresponds to a decrease in $\Delta G^{\neq}$. Thus, the HL electrolyte effectively reduces the energy barrier for the Zn/Zn^{2+} oxidizing reaction via interfacial chemisorption, dynamically facilitating the dissolution process (Figure 5d).

To further clarify the chemical evolution at the Zn interface, the formation mechanism of the SEI was theoretically explored. According to DFT calculations (Figure 5e), the higher highest occupied molecular orbital (HOMO) energy level of LS compared to H_2O indicates its greater ease of losing electrons. Concurrently, its lower lowest unoccupied molecular orbital (LUMO) energy level implies superior reducibility under cathodic potentials. Consequently, these distinct electronic structure features lead to the preferential decomposition of LS during the charge-discharge process. Based on its molecular structure comprising guaiacyl and syringyl units, LS undergoes sequential redox reactions at the electrode interface (Figure 5f) [37]. Phenolic hydroxyl groups are oxidized into semiquinone radicals, which are subsequently converted into quinone (Q) species. Aromatic ring cleavage then occurs, yielding carboxylic acids that undergo decarboxylation to ultimately form $ZnCO_3$. Concurrently, $-SO_3^-$ can be partially reduced to S^{2-} under cathodic conditions, leading to the formation of ZnS deposits. Notably, catechol-like intermediates derived from LS decomposition can enhance interfacial adhesion between the Zn anode and hydrogel electrolyte through surface coordination.

In the early stage, the regulation of Zn stripping behavior mainly relies on the homogenizing effect of LS on stripping energy. Once the SEI is formed, LS molecules lose direct interaction with the Zn anode. Fortunately, the formed SEI and the ANF-PVA hydrogel can continue to regulate the deposition and stripping behavior of Zn. The SEI forms during Zn deposition process and thus significantly influences Zn nucleation. As illustrated in Figure 5g, Zn nucleation within LE follows the 3D instantaneous mode, indicating that limited nucleation sites emerge only at the initial stage, which consequently leads to subsequent uneven deposition. For the HL system, the current density first decreases, corresponding to the reduction of LS to form the SEI layer. Subsequently, the current density curve transitions to 3D progressive mode, during which new nucleation sites continuously emerge. The preceding spectroscopic characterizations have fully confirmed that the SEI is rich in $-SO_3^-$ groups, and the LS primarily relies on sulfonate groups adsorbing onto the Zn surface to modulate the stripping energy barrier. Therefore, it is reasonable to hypothesize that the pre-formed SEI can induce grain-oriented Zn stripping, which is consistent with the electrode morphology observed after multiple cycle operations. When assembled into symmetric cells, Zn electrodes with a pre-formed SEI exhibit stable charge-discharge profiles and uniform deposition morphology, confirming the influence of the SEI on plating/stripping behavior (Figures S37, S38).

Collectively, as illustrated in Figure 5h, the interfacial regulation mechanism of the HL involves two dynamic processes: (i) Adsorption and stripping stage: LS molecules preferentially adsorb onto the Zn surface to form an initial organic layer that induces interfacial charge redistribution and facilitates grain-oriented Zn stripping. (ii) Deposition and SEI formation stage: During Zn^{2+} reduction, LS molecules continuously decompose to form a SEI layer comprising a mixture of organic and inorganic species. This in situ formed SEI simultaneously suppresses parasitic reactions and guides homogeneous Zn nucleation beneath the layer, leading to dense and reversible Zn stripping/plating.

2.5 | Electrochemical Performance of HL

HL electrolyte facilitates the uniform stripping and plating processes, endowing the system with outstanding electrochemical performance. As revealed by the linear sweep voltammetry (Figure S39), the onset potential for HER in HL is positively shifted compared to that in LE, which can be attributed to the modified solvation structure and reduced hydrogen bonding. Moreover, the higher nucleation overpotential in HL promotes the formation of more nucleation sites with smaller radii, thereby improving deposition uniformity (Figure 6a). The lower activation energy derived from the Nyquist plots facilitates the fast desolvation process (Figures 6b,S40). These electrochemical characterizations have confirmed the significant potential of HL for use in high-performance AZIBs. To evaluate the effect of HL on the plating/stripping reversibility of Zn anodes, Zn||Cu asymmetric cells were assembled to measure the CE (Figure 6c). Under the conditions of 10 mA cm^{-2}/1 mAh cm^{-2}, the Zn|HL|Cu cell maintained an average CE of 99% over 720 cycles, whereas the Zn|LE|Cu cell experienced a short circuit after only 120 cycles. When ANF-PVA or LS is used individually, their CE values reach only 200 and 100 cycles, respectively, which are considerably lower than that of HL. This result quantitatively confirms a strong synergistic effect between ANF-PVA and LS (Figure S41). In addition, the Zn|HL|Zn symmetric cell demonstrated exceptional long-term cycling durability at room temperature (25 °C), with stable operation over 5000 h at 2 mA cm^{-2} and 1 mAh cm^{-2} (Figure S42). Even under harsh conditions of 5 mA cm^{-2}/5 mAh cm^{-2} and 10 mA cm^{-2}/10 mAh cm^{-2} (Figures 6d,S43), the cell consistently delivered extended lifespans of 1250 h and 500 h, respectively, significantly outperforming the Zn|LE|Zn cell. This high reversibility is attributed to the effective regulation of Zn deposition/stripping behavior by HL. XRD patterns of soaked Zn foils (Figure S44) showcase that HL successfully suppresses the generation of byproducts, crucial for long-cycle stability. When cycled at a high depth of discharge to 60% (Figure S45), the cell equipped with LE failed to cycle continuously due to uncontrolled dendrite growth and Zn^{2+} depletion. In contrast, the HL-based cell maintained stable cycling for 250 h, demonstrating its promise for high-Zn-utilization anodes. Rate capability tests also underscored HL's enhancement in electrochemical performance: as current density increased from 1 to 50 mA cm^{-2}, the HL cell remained stable, while the LE cell short-circuited within 20 h (Figure 6e). For aqueous batteries, the reliable low-temperature operation is critical for applications in cold climates or specialized environments. As corroborated by the aforementioned differential scanning calorimetry tests and MD simulations, the HL electrolyte holds great potential for superior low-temperature performance. Encouragingly, the HL-based symmetric cell delivers an ultralong cycle life exceeding 10 900 h at −40 °C under current densities of 0.2 and 0.5 mA cm^{-2} (Figures 6f,S46), and even maintains stable cycling for over 500 h at a higher current density of 1.0 mA cm^{-2} (Figure S47). The outstanding low-temperature performance of the HL electrolyte mainly originates from two aspects. On the one hand, the strong interactions between the polar groups in the ANF-PVA hydrogel and the LS with water molecules effectively disrupt the long-range hydrogen-bonding network of bulk water, thereby inhibiting its crystallization. On the other hand, the three-dimensional porous framework of the ANF-PVA hydrogel spatially confines water molecules, rendering the nucleation and growth of large ice crystals difficult. Moreover, the Zn electrodes cycled in the HL electrolyte at low temperatures exhibits a uniform deposition/stripping morphology without the formation of byproducts (Figure S48), all of which contribute to its ultralong cycle life under low-temperature conditions. A comprehensive performance comparison (Figure 6g) indicates that the HL system outperforms most reported hydrogel electrolytes (Table S1) [32, 38–47], highlighting its strong potential for protecting Zn anodes and promoting the commercialization of high-stability aqueous batteries.

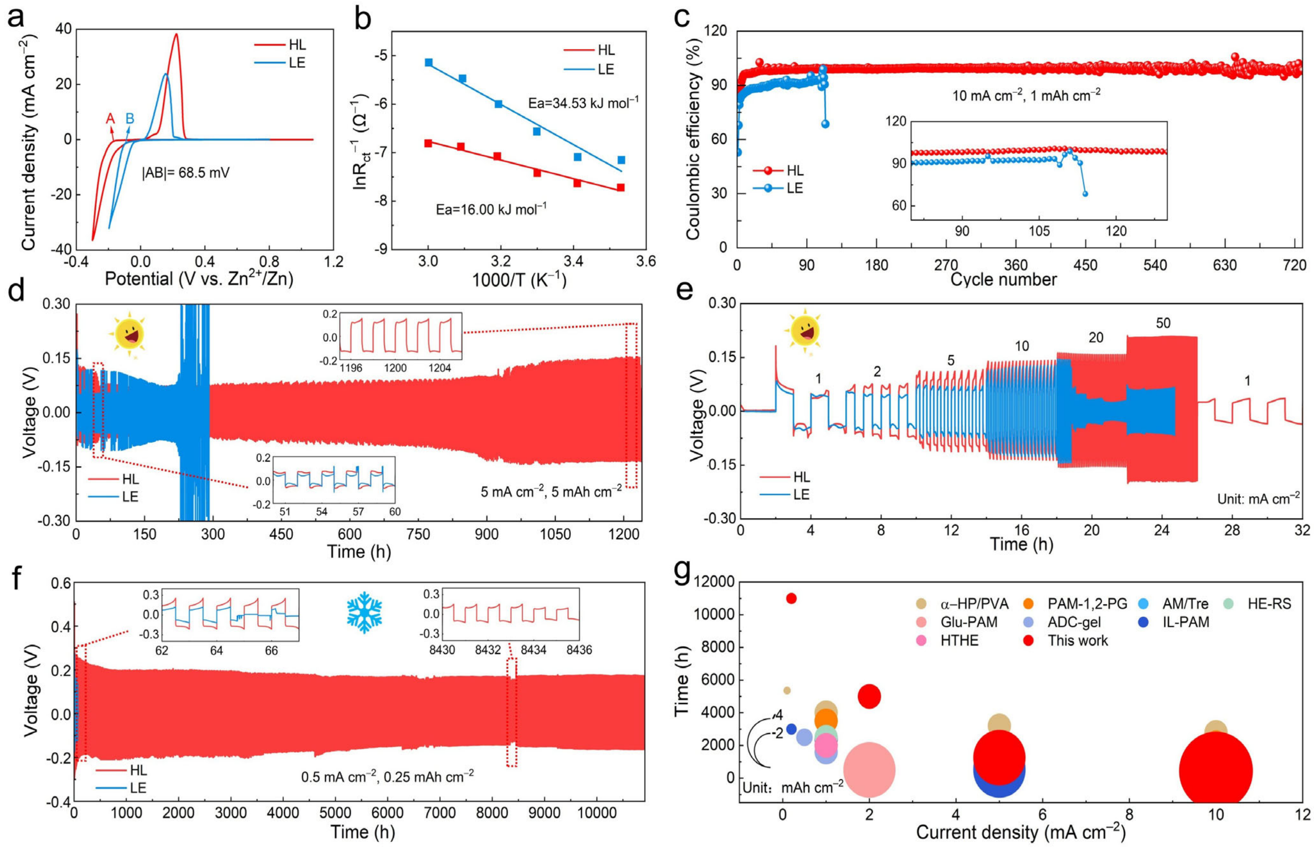

FIGURE 6 | Electrochemical performances. (a) CV curves of Zn||Ti asymmetric cells. (b) Arrhenius plots and comparison of activation energies for different electrolytes. (c) CE of Zn stripping/plating for Zn||Ti cells. (d) long-term galvanostatic cycling for symmetric cells at 5.0 mA cm^{-2}/5.0 mAh cm^{-2}; Inset: Detailed voltage profiles at specific cycling duration. (e) Rate capability at various current densities. (f) Long-term galvanostatic cycling of symmetric cells at a temperature of −40 °C. (g) Lifespan comparison between this work and recently reported studies.

2.6 | AZIB Full Cell Performance

Finally, to evaluate the feasibility of the HL electrolyte, Zn||I_2 full cells were assembled with an iodine cathode (Figure 7a). Electrochemical impedance spectroscopy revealed that the Zn|HL|I_2 configuration exhibited a lower impedance than its LE-based counterpart (Figure S49), indicating reduced charge-transfer resistance. This advantage translated into enhanced reaction kinetics and superior reversibility, as evidenced by the highly stable and overlapping CV profiles of the HL-based system over three cycles at 0.5 mV s^{-1}, in stark contrast to the LE-based cell (Figures 7b,S50). Consequently, during rate capability tests from 0.5 to 10 A g^{-1} (Figures 7c,d, and S51), the cell employing HL electrolyte consistently delivered higher capacities and improved stability across all current densities. Furthermore, it also demonstrated excellent long-term cycling stability (Figure 7e). At a current density of 5 A g^{-1}, the Zn|HL|I_2 cell retained 78.2% of its capacity after 20 000 cycles and continued to operate stably for over 30 000 cycles. By contrast, the Zn|LE|I_2 counterpart suffered from rapid capacity decay and failed after only 4800 cycles. To further probe its robustness under low negative-to-positive capacity ratio (N/P) conditions, Zn||I_2 cells with high mass loading and a thin Zn anode were tested. Remarkably, under a N/P of 5, the HL-based system delivered an initial capacity of 163.3 mAh g^{-1} and still maintained 125.5 mAh g^{-1} after 2000 cycles (Figure S52). Even at −40 °C, the Zn|HL|I_2 cell demonstrated outstanding stability (Figure 7f). Subsequent differential electrochemical mass spectrometry (DEMS) analyses (Figures 7g,S53) confirmed the effective HER suppression by HL, where the corresponding signal readily decreased and stabilized. This is in sharp contrast to the persistent hydrogen evolution observed in LE. As a practical demonstration, a pouch-type Zn|HL|I_2 battery was fabricated, which successfully powered a timer during repeated bending and cutting tests (Figure S54). More encouragingly, the pouch cell retained 87.3% of its initial capacity after 200 cycles, underscoring its excellent cycling durability (Figure 7h). Collectively, the HL electrolyte plays a vital role in stabilizing the Zn/electrolyte interface and extending the lifespan of full cells under various operational conditions, highlighting its potential to accelerate the commercialization of AZIBs.

3 | Discussion

In summary, a multifunctional HL electrolyte was developed to enable bidirectional regulation of Zn stripping and plating behavior. In this electrolyte, the ANF-PVA network primarily serves to homogenize the electric field distribution, thereby improving the kinetics of Zn stripping. Meanwhile, the added LS additive helps to uniformize the stripping energy. Under the synergistic regulation of both components, grain-oriented stripping was successfully achieved. Furthermore, the in situ decomposition

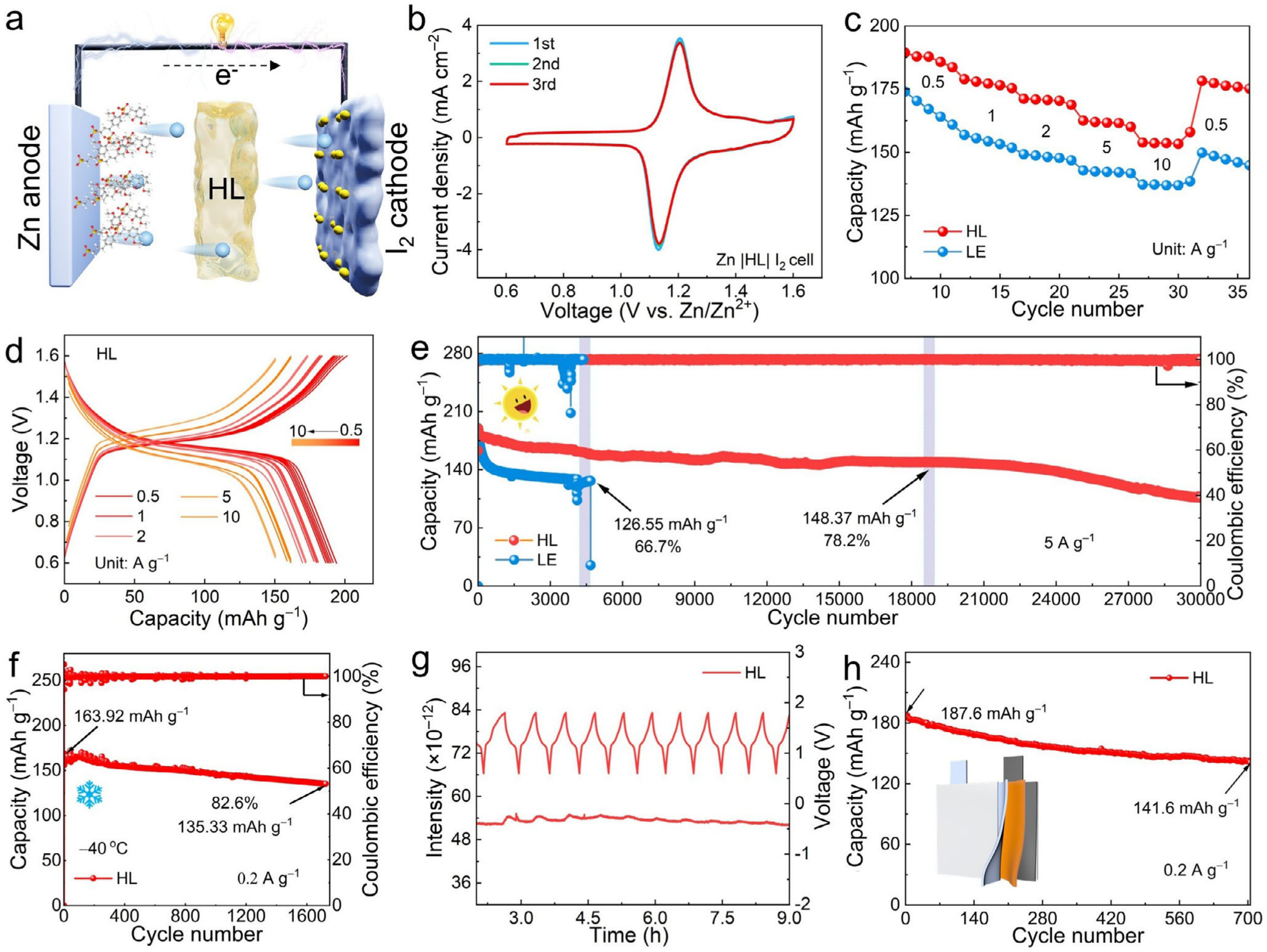

FIGURE 7 | Electrochemical performances of Zn||I_2 full cells. (a) Schematic diagram for full cell. (b) CV curves for full cells with HL electrolyte. (c) Rate performance. (d) The galvanostatic charge/discharge profiles of Zn||I_2 full cell equipped with HL electrolyte. Long-term cycling performance of Zn||I_2 full cells employing HL electrolyte under (e) 25 °C and (f) −40 °C. (g) DEMS pattern of Zn||I_2 cells with HL electrolyte. (h) Cycling performance of pouch cell.

of LS generates a composite SEI layer enriched with organic phases, which further sustains the grain-oriented stripping and guides homogeneous Zn deposition. Consequently, the Zn||Zn symmetric cell delivers an ultralong cycling lifespan of 1250 h at 5 mA cm^{-2} and 5 mAh cm^{-2}, while the Zn||I_2 full cell maintains 78.2% of its capacity over 20 000 cycles. Notably, stable operation is retained even under extreme low-temperature conditions of −40 °C. This work offers a comprehensive understanding of grain-oriented Zn dissolution, providing valuable insights for the design of pragmatic AZIBs.

Author Contributions

Zixing Dong: conceptualization, data curation, methodology, and writing – original draft. **Shige Wang**: conceptualization, methodology. **Jiashu Chen**: software, data curation. **Qianwei Huang**: methodology. **Haoqing Ji**: software, data curation. **Jun Peng**: software, data curation. **Huakun Liu**: funding acquisition, supervision. **Jingyu Sun**: writing – review and editing. **Shixue Dou**: funding acquisition, writing – review and editing. **Lizhi Xu**: methodology, resources. **Zaiping Guo**: writing – review and editing, supervision. **Chao Wu**: data curation, supervision, and writing – review and editing. **Xianzhong Yang**: conceptualization, supervision, methodology, funding acquisition, and writing – review and editing.

Acknowledgments

This work was supported by the National Natural Science Foundation of China (52302289 and 22379097). The authors also acknowledge support from Institute of Energy Materials Science (IEMS), Shanghai, China. Received: (will be filled in by the editorial staff)

Conflicts of Interest

The authors declare no conflicts of interest.

Data Availability Statement

The data that support the findings of this study are available from the corresponding author upon reasonable request.

References

1. W. Gu, K. Wu, J. W. Huang, et al., “The Role and Mechanism of Separators in Aqueous Zinc Metal Batteries: A Critical Review,” *Advanced Energy Materials* 15 (2025): 2502652, https://doi.org/10.1002/aenm.202502652.

2. Z. Wang, J. Huang, Z. Guo, et al., "A Metal-Organic Framework Host for Highly Reversible Dendrite-Free Zinc Metal Anodes," *Joule* 3 (2019): 1289–1300, https://doi.org/10.1016/j.joule.2019.02.012.

3. X. W. Jiang, Y. D. Wang, W. F. Li, et al., "High-Performance Zn–I_2 Batteries Enabled by Porous Hetero-Carbon Nanofiber Hosts with TiO_2 Homojunctions," *Advanced Fiber Materials* 8 (2025): 87–98, https://doi.org/10.1007/s42765-025-00595-w.

4. K. C. Matthews, B. Rush, R. Gearba, X. Guo, G. Yu, and J. H. Warner, "Cryo-Electron Microscopy Reveals Na Infiltration into Separator Pore Free-Volume as a Degradation Mechanism in Na Anode: Liquid Electrolyte Electrochemical Cells," *Advanced Materials* 36 (2024): 2308711, https://doi.org/10.1002/adma.202308711.

5. T. Huang, K. Xu, N. Jia, et al., "Intrinsic Interfacial Dynamic Engineering of Zincophilic Microbrushes via Regulating Zn Deposition for Highly Reversible Aqueous Zinc Ion Battery," *Advanced Materials* 35 (2023): 2205206, https://doi.org/10.1002/adma.202205206.

6. D. Wang, H. Liu, D. Lv, C. Wang, J. Yang, and Y. Qian, "Rational Screening of Artificial Solid Electrolyte Interphases on Zn for Ultrahigh-Rate and Long-Life Aqueous Batteries," *Advanced Materials* 35 (2023): 2207908, https://doi.org/10.1002/adma.202207908.

7. K. Wang, F. Zhang, X. W. Jiang, et al., "Bionic Nanogel Interfaces Unlock Long-Term Stability in Zn Metal Electrodeposition-Based Electrochromic Windows," *Advanced Materials* 37 (2025): e09980, https://doi.org/10.1002/adma.202509980.

8. D. Wang, S. Hu, T. Li, et al., "Anti-Dendrite Separator Interlayer Enabling Staged Zinc Deposition for Enhanced Cycling Stability of Aqueous Zinc Batteries," *Nature Communications* 16 (2025): 259, https://doi.org/10.1038/s41467-024-55153-6.

9. Z. J. Zhao, Y. G. Liao, S. K. Li, et al., "Scalable Zn-Alloy Anode for High-Current-Density Aqueous Zinc-Ion Batteries," *Advanced Functional Materials* 36 (2026): e20763, https://doi.org/10.1002/adfm.202520763.

10. J. Li, A. Azizi, S. Zhou, et al., "Hydrogel polymer electrolytes toward better zinc-ion batteries: A comprehensive review," *eScience* 5 (2025): 100294, https://doi.org/10.1016/j.esci.2024.100294.

11. Z. Dong, C. Zhong, H. Chai, et al., "Emerging in Situ Thermal Treatment Strategies for Tailoring Uniform Zn Deposition Toward Stable Zn Anodes," *Advanced Functional Materials* 35 (2025): 2503502, https://doi.org/10.1002/adfm.202503502.

12. X. Feng, H. Fang, N. Wu, et al., "Review of Modification Strategies in Emerging Inorganic Solid-State Electrolytes for Lithium, Sodium, and Potassium Batteries," *Joule* 6 (2022): 543–587, https://doi.org/10.1016/j.joule.2022.01.015.

13. L. Zhang, J. Xiao, X. Xiao, et al., "Molecular Engineering of Self-assembled Monolayers for Highly Utilized Zn Anodes," *eScience* 4 (2024): 100205, https://doi.org/10.1016/j.esci.2023.100205.

14. H. Guo, H. Luo, F. Zhu, et al., "Mechanical-Thermal Decoupling Engineering Unlocks Ultra-Stable Dry Thick Iodine Cathodes for Ah-Level Zinc-Based Pouch Batteries," *Advanced Materials* (2026), https://doi.org/10.1002/adma.73037.

15. X. Yang, Z. Dong, G. Weng, et al., "Crystallographic Manipulation Strategies Toward Reversible Zn Anode With Orientational Deposition," *Advanced Energy Materials* 14 (2024): 2401293, https://doi.org/10.1002/aenm.202401293.

16. C. Zhong, Y. Wang, M. Yu, et al., "Epitaxial Electrodeposition for Stable Zn Anodes: Mechanisms, Strategies, and Prospects," *Advanced Functional Materials* (2026), https://doi.org/10.1002/adfm.75291.

17. C. Xie, S. Liu, Z. Yang, et al., "Discovering the Intrinsic Causes of Dendrite Formation in Zinc Metal Anodes: Lattice Defects and Residual Stress," *Angewandte Chemie International Edition* 62 (2023): e202218612, https://doi.org/10.1002/ange.202218612.

18. Z. Liu, Z. Guo, L. Fan, et al., "Construct Robust Epitaxial Growth of (101) Textured Zinc Metal Anode for Long Life and High Capacity in Mild Aqueous Zinc-Ion Batteries," *Advanced Materials* 36 (2024): 2305988, https://doi.org/10.1002/adma.202305988.

19. H. Meng, Q. Ran, T.-Y. Dai, et al., "Lamellar Nanoporous Metal/Intermetallic Compound Heterostructure Regulating Dendrite-Free Zinc Electrodeposition for Wide-Temperature Aqueous Zinc-Ion Battery," *Advanced Materials* 36 (2024): 2403803, https://doi.org/10.1002/adma.202403803.

20. Z. Hao, Y. Zhang, Z. Hao, et al., "Metal Anodes with Ultrahigh Reversibility Enabled by the Closest Packing Crystallography for Sustainable Batteries," *Advanced Materials* 35 (2023): 2209985, https://doi.org/10.1002/adma.202209985.

21. C. Yang, P. Woottapanit, S. Geng, et al., "Highly Reversible Zn Anode Design through Oriented ZnO(002) Facets," *Advanced Materials* 36 (2024): 2408908, https://doi.org/10.1002/adma.202408908.

22. X. Yang, J. Lv, C. Cheng, et al., "Mosaic Nanocrystalline Graphene Skin Empowers Highly Reversible Zn Metal Anodes," *Advanced Science* 10 (2023): 2206077, https://doi.org/10.1002/advs.202206077.

23. Y. Su, B. Chen, Y. Sun, et al., "Rationalized Electroepitaxy Toward Scalable Single-Crystal Zn Anodes," *Advanced Materials* 35 (2023): 2301410, https://doi.org/10.1002/adma.202301410.

24. Z. P. Liu, G. N. Xu, Y. Zhang, et al., "Unveiling Zinc Stripping and Molecular Engineering for High-Performance Zinc Anode," *Angewandte Chemie International Edition* 64 (2025): e202501960, https://doi.org/10.1002/ange.202501960.

25. D. Meng, X. Liang, Q. Liu, et al., "An Electrostripping Strategy for Constructing a 3D Honeycomb-Like Zn Anode Toward Dendrite-Free Zinc-Ion Batteries," *Advanced Functional Materials* 34 (2024): 2411047, https://doi.org/10.1002/adfm.202411047.

26. Y. Wang, C. Zhong, C. Li, et al., "Alloying Strategies for Stable Zn Anodes: Mechanistic Insights and Design Principles," *ACS Nano* 20 (2026): 119–136, https://doi.org/10.1021/acsnano.5c18604.

27. R. T. Guo, X. Liu, K. Ni, et al., "Non-Destructive Stripping Electrochemistry Enables Long-Life Zinc Metal Batteries," *Energy & Environmental Science* 18 (2025): 2353–2364, https://doi.org/10.1039/D4EE05044D.

28. J. C. Zhang, Z. P. Liu, M. Li, et al., "Synchronized Regulating Zn^{2+} Depositing/Stripping Processes to Achieve Ultra-Stable Aqueous Zinc Metal Batteries," *Energy Storage Mater* 81 (2025): 104451, https://doi.org/10.1016/j.ensm.2025.104451.

29. L. Xu, X. Zhao, C. Xu, and N. A. Kotov, "Water-Rich Biomimetic Composites with Abiotic Self-Organizing Nanofiber Network," *Advanced Materials* 30 (2017): 1703343, https://doi.org/10.1002/adma.201703343.

30. H. Zhang, W. B. Jia, M. Z. Sun, et al., "High-strength and fracture-resistant ionogels via solvent-tailored interphase cohesion in nanofibrous composite networks,"*Science Advances* 11 (2025): eaea6883, https://doi.org/10.1126/sciadv.aea6883.

31. W. Zhou, Z. Chen, S. Zhao, M. Liu, and S. Chen, "Lignin-Derived Polyanionic Crosslinked Gel Interfacial Layer with Ion-Sieving and Ion-Regulating Capabilities for Dendrite-Free Zinc Anodes," *Angewandte Chemie International Edition* 64 (2025): e202508359, https://doi.org/10.1002/ange.202508359.

32. S. J. Guo, M. Y. Yan, D. M. Xu, et al., "Anti-Freezing Hydrogel Electrolyte with a Regulated Hydrogen Bond Network Enables High-Rate and Long Cycling Zinc Batteries," *Energy & Environmental Science* 18 (2025): 418–429, https://doi.org/10.1039/D4EE02772H.

33. Q. Wang, J. Huang, L. Qi, et al., "A Bioinspired Gradient Hydrogel Electrolyte Network With Optimized Interfacial Chemistry Toward Robust Aqueous Zinc-Ion Batteries," *ACS Nano* 19 (2025): 26770–26781, https://doi.org/10.1021/acsnano.5c06914.

34. Y. Zhang, X. Zheng, K. Wu, et al., "Nonionic Surfactant-Assisted in Situ Generation of Stable Passivation Protective Layer for Highly Stable Aqueous Zn Metal Anodes," *Nano Letters* 22 (2022): 8574–8583, https://doi.org/10.1021/acs.nanolett.2c03114.

35. L. H. Chang, S. Y. Bi, J. M. Li, Q. C. Sun, X. G. Lu, and H. W. Cheng, "Manipulating Bilateral Interface Chemistry via Multifunctional Salt Additive for Durable Aqueous Zinc Batteries," *ACS Nano* 19 (2025): 27424–27439, https://doi.org/10.1021/acsnano.5c05592.

36. Y. Zhao, Z. Chen, X. Gao, et al., "In Situ Self-Respiratory Solid-to-Hydrogel Electrolyte Interface Evoked Well-Distributed Deposition on Zinc Anode for Highly Reversible Zinc-Ion Batteries," *Angewandte Chemie International Edition* 64 (2024): e202415251, https://doi.org/10.1002/ange.202415251.

37. J. Shen, M. Cai, G. Li, C. F. Guo, X. Qiu, and Y. Qian, "Lignosulfonate-Derived Conducting Organohydrogel as Anisotrpic Bioadhesive for Motion-Artifact-Free Epidermal Bioelectronics," *Advanced Functional Materials* 35 (2024): 2413597, https://doi.org/10.1002/adfm.202413597.

38. X. Y. Xu, S. M. Li, S. B. Yang, and B. Li, "Superelastic Hydrogel Electrolyte Incorporating Helical Protein Molecules as Zinc Ion Transport Pathways to Enhance the Cycling Stability of Zinc Metal Batteries," *Energy & Environmental Science* 17 (2024): 7919–7931, https://doi.org/10.1039/D4EE02510E.

39. S. Yang, Q. Wu, Y. Li, et al., "A Bio-Inspired Multifunctional Hydrogel Network with Toughly Interfacial Chemistry for Dendrite-Free Flexible Zinc Ion Battery," *Angewandte Chemie International Edition* 63 (2024): e202409160, https://doi.org/10.1002/ange.202409160.

40. H. Tian, M. Yao, Y. Guo, et al., "Hydrogel Electrolyte with Regulated Water Activity and Hydrogen Bond Network for Ultra-Stable Zinc Electrode," *Advanced Energy Materials* 15 (2025): 2403683, https://doi.org/10.1002/aenm.202403683.

41. Y. F. Wang, L. Mo, X. X. Zhang, et al., "Regulating Water Activity for All-Climate Aqueous Zinc-Ion Batteries," *Advanced Energy Materials* 14 (2024): 2402041, https://doi.org/10.1002/aenm.202402041.

42. Q. He, G. Z. Fang, Z. Chang, et al., "Building Ultra-Stable and Low-Polarization Composite Zn Anode Interface via Hydrated Polyzwitterionic Electrolyte Construction," *Nano-Micro Letters* 14 (2022): 93, https://doi.org/10.1007/s40820-022-00835-3.

43. W. Y. Zhu, Z. Y. Lei, and P. Y. Wu, "Multi-Stage Collaborative Design of Hierarchical Twisted Hydrogel Electrolytes for Aqueous Zinc-Ion Batteries with High Capacity, Ultralong Stability, and Mechanical Robustness," *Energy & Environmental Science* 18 (2025): 3647–3658, https://doi.org/10.1039/D5EE00001G.

44. C. Yan, L. Zhu, P. Li, et al., "Multi-Level Zn^{2+} -Buffering Interphase Enabled by Hierarchical Nanostructure Engineering of Gel Polymers for Highly Reversible Zinc Metal Anode," *Advanced Materials* 38 (2026): e15316, https://doi.org/10.1002/adma.202515316.

45. Y. Lin, J. Huang, S. Wang, et al., "Stretchable, Adhesive, Anti-Freezing Hydrogel Electrolytes with Dual-Functional Water Regulation Enabled by Amide Group–Salt–Water Interactions for All-Climate Zinc-Ion Batteries," *Advanced Materials* 37 (2025): e09975, https://doi.org/10.1002/adma.202509975.

46. J. Peng, W. Song, W. Zhang, et al., "Bone-Inspired Sustainable Hydrogel Electrolytes for Zn Metal Batteries," *Angewandte Chemie International Edition* 64 (2025): e202506449, https://doi.org/10.1002/ange.202506449.

47. L. Gou, L. Zhu, W. Wang, et al., "From Physical Cross-Linking to Tailored Phosphorylation: Unlocking High-Performance and Biocompatible Xanthan-Konjac Hydrogels for Zinc-Ion Batteries," *Advanced Materials* 37 (2025): 2505132, https://doi.org/10.1002/adma.202505132.

Supporting Information

Additional supporting information can be found online in the Supporting Information section.

Supporting File: ange72506-sup-0001-SuppMat.docx.